Magnetic Resonance-Based Electric Properties Tomography via Green's Integral Identity

IEEE Access
Multidisciplinary ⋮ Rapid Review ⋮ Open Access Journal

Received 16 December 2024, accepted 20 February 2025, date of publication 26 February 2025, date of current version 12 March 2025.

Digital Object Identifier 10.1109/ACCESS.2025.3546036

RESEARCH ARTICLE

Magnetic Resonance-Based Electric Properties Tomography via Green's Integral Identity

LUCA ZILBERTI[1], ALESSANDRO ARDUINO[1], UMBERTO ZANOVELLO[1], JESSICA A. MARTINEZ[2], KEVIN MOULIN[3,4], ADRIANO TROIA[1], AND ORIANO BOTTAUSCIO[1]

[1]Istituto Nazionale di Ricerca Metrologica, 10135 Turin, Italy
[2]Department of Physics, University of Colorado, Boulder, CO 80309, USA
[3]CREATIS Laboratory, UJM-Saint-Etienne, INSA, CNRS UMR 5520, INSERM 1294, University of Lyon, 42023 Saint-Étienne, France
[4]Department of Radiology, University Hospital Saint-Étienne, 42270 Saint-Étienne, France

Corresponding author: Luca Zilberti (l.zilberti@inrim.it)

The results here presented have been developed in the framework of the EMPIR Project 18HLT05 QUIERO. This project 18HLT05 QUIERO has received funding from the EMPIR programme co-financed by the Participating States and from the European Union's Horizon 2020 research and innovation programme.

This work involved human subjects or animals in its research. Approval of all ethical and experimental procedures and protocols was granted by the CPP Nord Ouest VI under Application No. 2015-A01802-47 and the CPP Ile de France VIII under Application No. 19.02.22, and performed in line with the Declaration of Helsinki.

ABSTRACT A new approach to Magnetic Resonance-based Electric Properties Tomography (EPT) is presented. The method applies Green's integral identity to the equation that regulates the EPT problem. The resultant integral equations are used to impose the consistency of the measured values of the radiofrequency field. This is achieved by seeking dielectric properties values that allow satisfying the identity within suitable kernels of voxels. In each kernel, an overdetermined system of equations is written, and the corresponding problem is solved in the least squares sense, providing an index of trustworthiness of the solution. Both the complete formulation and its phase-based approximation are presented. The application of a filter, which post-processes the raw results based on the index of trustworthiness, is also discussed. The performance of the method is evaluated on synthetic data and experimental measurements acquired on a heterogeneous brain phantom and on four human volunteers. The reconstructions are compared to those produced through a Helmholtz-EPT with adaptive kernel. The new EPT method performs well in all tests.

INDEX TERMS Dielectric properties, electric properties tomography (EPT), Green identity, magnetic resonance imaging (MRI).

I. INTRODUCTION

Magnetic resonance-based Electric Properties Tomography (EPT) is a family of methods that aim to quantitatively map the dielectric properties of biological tissues, by exploiting data acquired through Magnetic Resonance Imaging (MRI) [1], [2], [3], [4]. EPT produces images of the electrical conductivity and, in some cases, of the dielectric permittivity (which is more challenging to reconstruct) at the Larmor frequency of the MRI scanner. The interest in these properties arises because of their potential use as biomarkers [5], [6], [7], [8], [9], [10]. More in general, the added value of EPT resides in the possibility to perform a pixel-wise absolute measurement of the target quantities. This feature should allow to objectively compare the outcomes of follow-up MRI exams carried out during longitudinal monitoring. EPT can also play a role in the framework of personalized medicine, providing useful information for optimizing the therapeutic plan of the patient [11], [12]. Additionally, EPT can be used for safety purposes, to estimate the Specific Absorption Rate (SAR) during an MRI scan, in a subject-specific way [13], [14], [15].

The EPT problem can be addressed with different approaches. Most methods elaborate on the transmit phase of the radiofrequency (RF) magnetic field. Other methods require the knowledge of the magnitude of the field. In some

The associate editor coordinating the review of this manuscript and approving it for publication was Jinhua Sheng.

cases, information about the incident fields produced by the scanner is also needed. The mathematical formulations can originate from differential or integral equations (see, for instance, [16] and [17], respectively). Direct or inverse algorithms can be adopted to get the solution. EPT can be performed at a local level (i.e., in the neighborhood of each single voxel), or on a global scale (on the whole target region at once). In addition to model-based techniques, EPT inference from the correlation of the dielectric properties with the water content [18] and data-driven EPT approaches [19] have also been proposed. A detailed analysis of the available EPT methods is beyond the scope of the present paper, but the reader can find it in some review articles [1], [2], [3], [4].

The most popular EPT approach, used as a term of reference in this paper, is Helmholtz-EPT (HH-EPT) [13]. HH-EPT is a local direct method, which elaborates either the complex map of the RF magnetic field or simply the phase of the field (in the latter case, reconstructing the conductivity only). HH-EPT is based on a straightforward formulation and makes use of relatively simple mathematical operations (mainly, the Laplacian operator, evaluated through a kernel of voxels surrounding the target voxel). Nevertheless, HH-EPT suffers from a couple of drawbacks, one related to the precision and the other to the accuracy of the EPT reconstruction. The first drawback is the amplification of the noise that affects the measured input data, caused by the evaluation of the second order derivatives in the Laplacian operator. This problem is usually managed by fitting the input data before calculating the derivatives. The effectiveness of this filter improves when extending the number of input data involved in the fitting, i.e., enlarging the kernel [20]. The other drawback happens when HH-EPT is applied at the interface between different tissues. Indeed, strictly speaking, the model behind HH-EPT is suitable to describe homogeneous regions and it is no longer rigorous if applied to heterogeneous structures. A "boundary error" may therefore affect the HH-EPT reconstruction if the calculation of the Laplacian involves voxels belonging to different tissues [21], [22]. These two issues have a conflicting nature: one compels to involve many points in the calculation (to filter the noise), whereas the other suggests using only the first neighbors of the target voxel (to limit the risk to cross a boundary). To handle this difficulty, in HH-EPT the kernels can be shaped in such a way to avoid crossing the interfaces between different tissues. This requires using a reference image, to identify the location of the interfaces.

To overcome the above drawbacks, we propose a different strategy, originating a novel, model-based, direct approach. This approach starts from the same equation used in HH-EPT but elaborates it through one of Green's identities, to get integral relationships. Once discretized, such relationships give rise to an algebraic problem, which allows calculating the dielectric properties. Due to the fundamental role played by the adopted Green's integral identity, the method will be abbreviated as Green-EPT.

Like HH-EPT, Green-EPT works within a kernel surrounding the target point. However, unlike HH-EPT, Green-EPT admits the possibility to assign different dielectric properties to each voxel in the kernel. Green-EPT also differs significantly from iterative methods, like [23], which make use of integral field equations involving the Green function. Green-EPT is a direct method; hence, from the computational viewpoint, it is simpler than iterative methods. Moreover, being model-based, it avoids possible biases that may be introduced during the training phase of data-driven approaches.

The paper is organized as follows. Section II presents the theory of the method and its implementation. Section III describes the numerical simulations and the experiments performed on a brain phantom and on four human volunteers. The results are illustrated in Section IV and discussed in Section V. Two appendices complement the paper: one illustrating the analytical equivalence between Green-EPT and HH-EPT in homogeneous regions, the other discussing an alternative version of Green-EPT.

II. THEORY

For the reader's convenience, subsections II-A and II-B summarize the physical background and the main features of a conventional HH-EPT approach. Subsections II-C, II-D, II-E and II-F describe the novelties introduced with the present work.

A. PHYSICAL BACKGROUND

Let Ω be a region (representing a portion of a human body that undergoes MRI) with homogeneous magnetic permeability μ_0, bounded by the closed surface $\partial\Omega$. In time-harmonic regime, the magnetic induction $\boldsymbol{B}$ and the electric field $\boldsymbol{E}$ satisfy Maxwell's equations

$$\nabla \times \boldsymbol{B} = \mu_0 (\sigma + \mathrm{j}\omega\varepsilon) \boldsymbol{E}, \tag{1}$$

$$\nabla \times \boldsymbol{E} = -\mathrm{j}\omega \boldsymbol{B}, \tag{2}$$

where j is the imaginary unit and ω is the angular frequency. The dielectric properties, that may change from point to point, are indicated by σ (electrical conductivity) and ε (permittivity). Due to the homogeneous permeability, vector $\boldsymbol{B}$ is continuous.

If we take the curl of (1), by virtue of the divergence-free character of $\boldsymbol{B}$, and using (2) to replace the curl of $\boldsymbol{E}$, we get

$$-\nabla^2 \boldsymbol{B} = \mu_0 \left[\nabla (\sigma + \mathrm{j}\omega\varepsilon) \times \boldsymbol{E} - \mathrm{j}\omega (\sigma + \mathrm{j}\omega\varepsilon) \boldsymbol{B} \right], \tag{3}$$

which, if we neglect the gradient of the dielectric properties (the so-called "local homogeneity assumption", LHA), reduces to

$$\nabla^2 \boldsymbol{B} = \mathrm{j}\omega\mu_0 (\sigma + \mathrm{j}\omega\varepsilon) \boldsymbol{B}. \tag{4}$$

Equation (4) is valid for homogeneous regions. Strictly speaking, it should not be used to describe regions where the dielectric properties may vary. In MRI, the scalar version of (4) holds for the transmit sensitivity B_1^+, [3], [4], i.e., the

positive circularly polarized component of the RF magnetic induction rotating at the Larmor angular frequency:

$$\nabla^2 B_1^+ = \mathrm{j}\omega\mu_0 \left(\sigma + \mathrm{j}\omega\varepsilon\right) B_1^+, \tag{5}$$

where

$$B_1^+ = \left|B_1^+\right| e^{\mathrm{j}\varphi^+} \tag{6}$$

is a complex quantity. We notice that, due to the LHA, the longitudinal component of $\boldsymbol{B}_1$ is left out of (5).

If the magnitude of B_1^+ is sufficiently homogeneous in the target region, (5) can be manipulated to obtain an approximated phase-based equation, relating the value of the conductivity to the phase of the field [1], [2], [3], [4]:

$$\nabla^2 \varphi^+ = \omega\mu_0\sigma. \tag{7}$$

When acceptable, this approximation allows avoiding the measurement of the magnitude of B_1^+.

B. PRELIMINARY REMARKS ON HELMHOLTZ-EPT

In standard HH-EPT, the dielectric properties of the target volume are deduced directly from (5), starting from the map of B_1^+. The latter is typically sampled on a regular grid of voxels, with finite size [1], [2], [3]. To mitigate the effect of the measurement noise, the sampled data are fitted, locally, with a paraboloid (see equation (A1) in Appendix A). The choice of the paraboloid is consistent with the simplified equation (7), which was derived under the LHA (hence, strictly speaking, for a region where the conductivity is homogeneous). For the sake of simplicity, the choice of the paraboloid is kept to produce a local approximation of the spatial distribution of the field regulated by (5). This operation is known as Savitzky–Golay filter [2], and requires that, for each target voxel, a kernel of surrounding voxels is involved in the fitting. Once the coefficients of the fitting have been identified, the Laplacian (which results to be constant in the kernel, by definition of the quadratic fitting function) is computed analytically and used to calculate the dielectric properties of the target voxel. In principle, the larger the size of the kernel, the better the filtering action. However, if the kernel is too large, the quadratic fitting might no longer provide a good approximation of the field distribution. A similar problem occurs if the kernel crosses the boundary between different materials. In this case, the quadratic fitting may deviate significantly from the actual field distribution. This situation produces a "boundary error" that, typically, manifests itself as a strong overshooting (or undershooting) of the dielectric properties associated with the kernel [1], [2]. As a result, the boundary error may compromise the reconstruction in the target voxel, even if it is not directly located along an interface (and therefore, theoretically speaking, should not suffer the effect of the LHA underlying (5)).

The solution of HH-EPT based on (7) is analogous to the solution described above starting from (5). Hence, the phase-based version of HH-EPT suffers from the same need to filter the measurement noise without introducing boundary errors.

To avoid the boundary errors, HH-EPT can take advantage of a tissue segmentation. For a given target voxel, the shape of the kernel that surrounds it can be adapted in such a way to avoid involving voxels that belong to another tissue [6], [24]. As an alternative, the shape of the kernel can be fixed, but the fitting can be calculated in a weighted way (the weights being proportional to the probability that the corresponding voxels belong to the same tissue as the target voxel) [25].

C. GREEN-EPT

Equation (5) is a Helmholtz equation. The solution of this equation, where B_1^+ is seen as an unknown, could be obtained by applying Green's identity, using a Green function that depends on the dielectric properties (see Appendix B).

Let us pretend, just for a while, that (5) is a Poisson equation

$$\nabla^2 B_1^+ = \zeta, \tag{8}$$

in which ζ is a known term that may vary from point to point.

For any interior point $P \in \Omega$, Green's integral identity [26] applied to (8) leads to

$$B_1^+(P) = \oint_{\partial\Omega} \left(\Psi \nabla B_1^+ \cdot \boldsymbol{n} - B_1^+ \nabla\Psi \cdot \boldsymbol{n}\right) ds - \int_\Omega \zeta\Psi\, dv, \tag{9}$$

where $\boldsymbol{n}$ indicates the normal unit vector directed outwards $\partial\Omega$ and $\Psi = 1/(4\pi r)$ is the Green function for the three-dimensional Poisson problem, in which r indicates the distance between P and any integration point. Unlike the Green function for the original Helmholtz problem, this Green function does not depend on the properties of the medium. Now, if we replace ζ with its explicit expression, we get

$$\begin{aligned} B_1^+(P) = &\oint_{\partial\Omega} \left(\Psi \nabla B_1^+ \cdot \boldsymbol{n} - B_1^+ \nabla\Psi \cdot \boldsymbol{n}\right) ds \\ &- \mathrm{j}\omega\mu_0 \int_\Omega \left(\sigma + \mathrm{j}\omega\varepsilon\right) B_1^+ \Psi\, dv. \end{aligned} \tag{10}$$

The unknown dielectric properties must have the value that allows balancing the left-hand side (i.e., the value of B_1^+ in P) and the right-hand side (i.e., the reconstruction obtained through the integrals). Appendix A discusses the analytical equivalence between (10) and the HH-EPT formulation.

Equation (10) is valid for homogeneous regions. In a realistic situation, Ω could be composed of different tissues. In this case, (4) no longer provides the rigorous description of the problem and the formulation is therefore affected by a model error. Being aware of this, we proceed heuristically, aiming at verifying, *a posteriori*, if the accuracy of our EPT reconstructions is satisfactory, despite the model error.

Making reference to a discretized structure, Ω will be a region composed of N_V voxels, playing the role of the kernel, and $\partial\Omega$ will be the external surface of this region, in turn discretized into N_S elementary rectangular faces. In the most general case, we could have a different value of conductivity and permittivity in each voxel within Ω. To match this

situation, the volume integral in (10) can be subdivided into N_V elementary contributions, involving N_V unknown values of complex conductivity ($\sigma + \mathrm{j}\omega\varepsilon$):

$$B_1^+(P) = \oint_{\partial\Omega} \left(\Psi \nabla B_1^+ \cdot \boldsymbol{n} - B_1^+ \nabla\Psi \cdot \boldsymbol{n}\right) ds - \mathrm{j}\omega\mu_0 \sum_{k=1}^{N_V} (\sigma + \mathrm{j}\omega\varepsilon)_k \int_{\Omega_k} B_1^+ \Psi \, dv. \quad (11)$$

Point P can be placed in the barycenter of each of the N_V voxels. By exploiting this degree of freedom, from (11) we can get a system of N_V complex equations, with N_V complex unknowns, whose solution gives the voxel-wise dielectric properties.

In a real case, a given kernel Ω will be composed of a relatively small number N_T of homogeneous biological tissues. By exploiting a reference image of the scanned region (which can be obtained through conventional MRI), the unknowns of the voxels that belong to the same tissue can be grouped. This reduces the number of unknowns in Ω (because $N_T < N_V$) and produces, for each kernel, an overdetermined system of equations, which can be solved in the least-square sense. As proved by the results, this strategy has the beneficial effect to stabilize the solution with respect to both the noise and the model error associated with the presence of the LHA. The larger the kernel, the more the system is overdetermined. On the other hand, the use of a small kernel limits the computational burden and makes the segmentation within each kernel easier. Hence, the size of the kernel should be chosen as a tradeoff between such requirements.

An alternative formulation of Green-EPT, which directly manages (5) as a Helmholtz equation, is described in Appendix B. Such an approach suffers some important drawbacks and therefore its detailed analysis is not pursued.

D. PHASE-BASED VERSION OF GREEN-EPT

Starting from (7), a phase-based version of Green-EPT can be developed using Green's integral identity:

$$\varphi^+(P) = \oint_{\partial\Omega} \left(\Psi \nabla\varphi^+ \cdot \boldsymbol{n} - \varphi^+ \nabla\Psi \cdot \boldsymbol{n}\right) ds - \omega\mu_0 \int_{\Omega} \sigma \Psi \, dv. \quad (12)$$

Equation (12) can be used to obtain, *mutatis mutandis*, an analogous version of (11), which provides a phase-based conductivity mapping. Unlike the complex version of the formulation, in this real version the volume integral involves the unknown conductivity and the Green function Ψ only.

The phase-based version of Green-EPT inherits most of the features of the complete version. Specifically, the calculation can be performed in a heterogeneous kernel. A stabilization of the results can be achieved forcing the unknowns of the voxels assigned to a given tissue to share the same value.

E. IMPLEMENTATION

In this Section we discuss practical aspects of the implementation of Green-EPT, summarized by the scheme at the top-left side of Fig. 1. Such aspects are discussed with reference to the general case, but they apply to the phase-based version as well.

As usually done for other EPT methods (including HH-EPT), when suitable symmetry conditions take place, the phase of B_1^+ is obtained as one half of the so-called transceive phase [1], [2], [3], [4], which can be acquired through MRI sequences of common use. This "transceive phase assumption" may influence the performance of the complex version of the formulation. On the contrary, the use in (7) of half the transceive phase, rather than the transmit phase, is rigorous [1], [2], [4].

The easiest way to implement the calculation in (11) is to assume that the value of B_1^+ is uniform inside each voxel and on each elementary surface element in which the boundary surface $\partial\Omega$ is discretized. The same applies, for the sake of simplicity, to the normal derivative of B_1^+ in the surface integral. Adopting this discretization scheme, we get

$$B_1^+(P) = \sum_{h=1}^{N_S} \left[\left(\nabla B_1^+ \cdot \boldsymbol{n}\right)_h \int_{\partial\Omega_h} \Psi \, ds - B_{1,h}^+ \int_{\partial\Omega_h} \nabla\Psi \cdot \boldsymbol{n} ds \right] - \mathrm{j}\omega\mu_0 \sum_{k=1}^{N_V} (\sigma + \mathrm{j}\omega\varepsilon)_k B_{1,k}^+ \int_{\Omega_k} \Psi \, dv, \quad (13)$$

in which the point where B_1^+ and its normal derivative are evaluated is implied by the integral that they multiply. In (13), the integrals involve geometric quantities only, and can be performed numerically, *a priori*.

Starting from a sampled distribution of B_1^+, the value associated with the surface element $\partial\Omega_h$ can be obtained as the average of the B_1^+ values in the barycenter of the two voxels sharing face $\partial\Omega_h$. Similarly, the normal derivative of B_1^+ on the h-th surface element can be calculated as the incremental ratio between the same two values. We notice that these calculations require the knowledge of B_1^+ in an extra layer of voxels surrounding the kernel of interest. Once calculated, the summation over the surface elements becomes part of the known term of the problem, together with $B_1^+(P)$. Instead, the elementary volume integrals produce the entries of the system matrix. All voxels in Ω participate, through the volume integral, at the calculation associated with a given reference point P. Thus, the system matrix associated with a given kernel is full. In Ω, clusters of uniform dielectric properties are created based on a reference image, cropped in the kernel under investigation. Typically, the reference image is the magnitude of the MR image used to get the transceive phase, so that the total acquisition time required by EPT is kept short and no registration between the reference and the phase images is needed. To create the clusters, an initial guess value for N_T is set, and the k-means algorithm available within MATLAB is applied (complete documentation about this function is available on The MathWorks website). If the distance between the mean contrasts of any pair of clusters is lower than a preset threshold, the algorithm is applied again, reducing N_T. The pseudocode that lists the operations

performed to create the clusters of unknowns is provided within Fig. 1.

The resulting overdetermined system (matrix A, with dimension $N_V \times N_T$) is solved in the least squares sense:

$$\min_x \|Ax - b\|^2, \tag{14}$$

where x is the array containing the N_T unknowns (one for each cluster in the kernel), b is the array containing the N_V known terms (one for each equation), and $\|\cdot\|$ denotes the quadratic norm. Matrix A is complex in the complete version of Green-EPT, and real in the phase-based version. In each kernel, noise, model errors, and segmentation errors, always contribute to a non-null residual ρ after the minimization in (14). An index of goodness of the solution can be obtained through the normalization

$$\chi^2 = \frac{\|\rho\|^2}{N_V - N_T}. \tag{15}$$

The latter can be ''propagated'' to the elements of x, according to the law of propagation of the uncertainty [27]. This allows obtaining, for each unknown, an index of trustworthiness T. The whole procedure is described in details in [28].

To create the EPT map, a parallelepiped-shaped kernel is placed in all admissible positions within the domain. This implies that each voxel participates at N_K kernels (with N_K different from voxel to voxel, in general). For each voxel, an array with N_K values of complex conductivity is therefore obtained. The array with the corresponding N_K trustworthiness values is obtained as well. The weighted average of such complex conductivity values is calculated (using T values as weights) and assigned to the voxel. The final trustworthiness associated with the voxel is obtained (ignoring, for the sake of simplicity, the correlation between single conductivity values) as the sum of the elements in the trustworthiness array.

In the current implementation, the shape of the kernels is rigid. Specifically, it is a parallelepiped with edges L_x, L_y and L_z. If a kernel requires data from points that are out of the domain, the calculation is skipped. If this occurs to all kernels in which a given voxel is involved, such a voxel will not be displayed in the raw EPT map. For the reader's convenience, the pseudocode of the algorithm that perform Green-EPT is provided in Fig. 1.

F. POST-PROCESSING

For each voxel, the adopted post-processing requires considering a sphere around it, with a given diameter D. Inside the sphere, based on the reference image, the voxels in which the contrast with respect to the central voxel is lower than 10 % are selected. Then, the weighted average of the dielectric properties of the selected voxels is calculated (using T as a weight). The result provides the final value of the conductivity and permittivity assigned to the target voxel. A scheme of the post-processing is given on the top-right side of Fig. 1. For the reader's convenience, the pseudocode of the algorithm that post-processes the raw images is provided in the same figure. The results of HH-EPT undergo an analogous elaboration. In this case, the residual of the fitting is used to get T [28].

III. SIMULATIONS AND EXPERIMENTS

Green-EPT has been verified using a set of numerical simulations, one experiment on a heterogeneous phantom, and four experiments performed on human volunteers.

A. NUMERICAL SIMULATIONS

To test Green-EPT on synthetic data, an electromagnetic simulation was performed using the Sim4Life software [29]. The Duke model of the Virtual Population [30] was positioned inside a two-channel, 16-leg high-pass shielded birdcage body coil (diameter: 713 mm, height: 450 mm) tuned at 128 MHz. The axial position of the human model was selected to simulate brain imaging. The head of the model was discretized with a 1 mm isotropic mesh; a coarser mesh was adopted in the remaining parts of the body. The discretization of the whole domain required about $51{\cdot}10^6$ cells. The tissue electrical properties were assigned according to the IT'IS Foundation database [31]. The convergence criterion was set to -30 dB. The distributions of both B_1^+ and B_1^- (i.e., the negative circularly polarized component of the RF magnetic flux density) generated by the two ports were extracted on a $170 \times 130 \times 175$ regular grid of voxels, covering the brain region. These data were used to compute the transmit sensitivity and transceive phase produced by a quadrature RF coil used both in transmission and reception, which represent the inputs of the EPT algorithm. In addition, a synthetic T1-weighted brain image was generated as the signal produced by a GRE sequence with a 59° reference flip angle, 30 ms repetition time (TR) and null echo time (TE). The values of the longitudinal relaxation time T1 of the relevant brain tissues were preliminary deduced, by exploiting their correlation with the dielectric properties [18]. Because of the adopted TE, the image does not depend on transverse relaxation time T2. To obtain a more realistic reference image, without sharp separations between tissues, a Gaussian filter (standard deviation: 0.8, truncated at one standard deviation) was applied.

Zero-average Gaussian noise was added to the simulated transmit and receive sensitivities. This affected, in turn, the transceive phase map and the reference T1-weighted image. The noise standard deviation was computed according to three values of signal to noise ratio (SNR): 300, 150, and 50. The noise standard deviation was obtained dividing the average receive sensitivity on the central brain slice by the SNR. The generated noise was added to the real and imaginary part of the transmit and receive sensitivity. A more realistic noise simulation should mimic, separately, the different MR sequences applied for the transceive phase and transmit sensitivity acquisition. Nevertheless, the proposed simplified procedure produced all ingredients to perform a first test of the Green-EPT method.

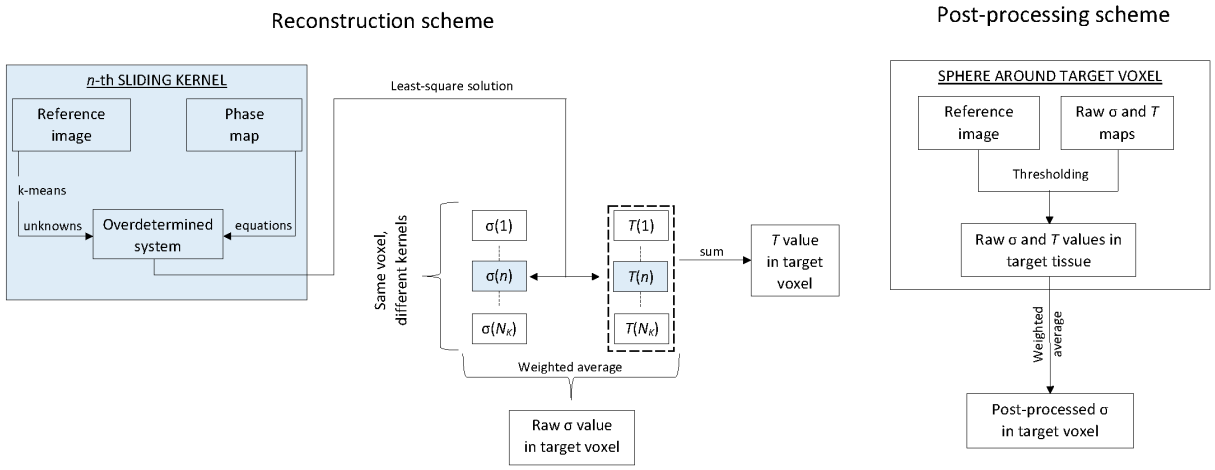

Algorithm 1 Identification of the clusters of unknowns in a kernel

Input: Maximum accepted number of clusters, N_T.
List of contrasts in the kernel, $\boldsymbol{m}$. Contrast threshold, t.
Output: List of cluster indices in the kernel, $\boldsymbol{c}$.

[$\boldsymbol{c}$, ***centroids***] ← kmeans($\boldsymbol{m}$, N_T) [MATLAB function kmeans]
$N_{T,new} \leftarrow N_T$
for $i = 2, \ldots, N_T$ **do**
  if ***centroids***(i) - ***centroids***(i - 1) < t **then**
    $N_{T,new} \leftarrow N_{T,new} - 1$
  end if
end for
[$\boldsymbol{c}$, ***centroids***] ← kmeans($\boldsymbol{m}$, $N_{T,new}$)
Return $\boldsymbol{c}$

Algorithm 3 Post-processing scheme

Input: Post-processing diameter D.
Reference image of contrasts.
Raw conductivity and trustworthiness maps.
Output: Post-processed conductivity map $\boldsymbol{\sigma}_{\text{avg}}$

for each voxel in the domain **do**
  Set j as the voxel index
  Select the voxels whose distance from the j-th is lower than $D/2$
  Among those, select the voxels whose contrast with respect the j-th is lower than 10 %
  Set $\boldsymbol{\sigma}$ as the list of conductivities in the selected voxels
  Set $\boldsymbol{T}$ as the list of trustworthiness values in the selected voxels
  $\boldsymbol{\sigma}_{\text{avg}}(j) \leftarrow \text{sum}(\boldsymbol{\sigma} .* \boldsymbol{T}) / \text{sum}(\boldsymbol{T})$ [MATLAB function sum]
end for
Return $\boldsymbol{\sigma}_{\text{avg}}$

Algorithm 2 Reconstruction scheme

Input: Sliding kernel size and shape. Reference image of contrasts.
Transceive phase map.
Output: Conductivity and trustworthiness values in each voxel, $\boldsymbol{\sigma}_{\text{avg}}$ and $\boldsymbol{T}_{\text{avg}}$.

Initialize to zero the output maps $\boldsymbol{\sigma}_{\text{avg}}$ and $\boldsymbol{T}_{\text{avg}}$.
for each kernel position **do**
  Apply **Algorithm 1** to get the list of cluster indices $\boldsymbol{c}$
  $N_T \leftarrow \max(\boldsymbol{c})$
  Set N_V as the number of voxels in the kernel
  Initialize matrix A with N_V rows and N_T columns
  Initialize vector b with N_V elements
  for $i = 1, \ldots, N_V$ **do**
    Set P as the barycenter of i-th voxel
    Update the i-th row of A with the discretized version of equation (12)
    Update the i-th element of b with the discretized version of equation (12)
  end for
  Set $\boldsymbol{x}$ as the solution to the least square problem (14)
  Set $\boldsymbol{t}$ as the trustworthiness vector computed according to [28]
  for $i = 1, \ldots, N_V$ **do**
    Set j as the global voxel index
    $\boldsymbol{\sigma}_{\text{avg}}(j) \leftarrow \boldsymbol{\sigma}_{\text{avg}}(j) + \boldsymbol{x}(\boldsymbol{c}(i)) * \boldsymbol{t}(\boldsymbol{c}(i))$
    $\boldsymbol{T}_{\text{avg}}(j) \leftarrow \boldsymbol{T}_{\text{avg}}(j) + \boldsymbol{t}(\boldsymbol{c}(i))$
  end for
end for
$\boldsymbol{\sigma}_{\text{avg}} \leftarrow \boldsymbol{\sigma}_{\text{avg}} ./ \boldsymbol{T}_{\text{avg}}$
Return $\boldsymbol{\sigma}_{\text{avg}}$, $\boldsymbol{T}_{\text{avg}}$

FIGURE 1. Main algorithms adopted in the proposed method, written with reference to the phase-based version of the technique. On top left, scheme of the Green-EPT reconstruction for the conductivity (σ) of a target voxel that participates at N_K kernels. Trustworthiness (T) is also obtained. On top right, scheme of the post-processing of the conductivity in a target voxel. Below the schemes, the pseudocodes of the algorithms that create the clusters of unknowns, perform the reconstruction, and post-process the image are reported.

B. EXPERIMENTS ON A HETEROGENEOUS BRAIN PHANTOM

A heterogeneous, anatomically realistic, brain-shaped phantom was realized, starting from the CAD of the brain of model 71 from the XCAT library (female, 27 years old, BMI = 18.6 kg/m^2) [32]. The external surfaces of the white matter (WM) and grey matter (GM) of this model were 3D-printed and used as molds. The material mimicking the WM was poured in the corresponding mold. Once gelled, the material was removed from the mold and placed within the larger GM mold. Finally, the material mimicking the GM was poured and gelled in direct contact with the WM gel. The tissue-mimicking materials were prepared following the recipe provided in [33], modified to also tune the relaxation times [34]. Samples of the materials were characterized, at 123 MHz, using a commercial open-ended coaxial probe. At 24 °C, the conductivity of the GM and WM gels resulted to be 0.59 S/m and 0.29 S/m, respectively. For both materials, the estimated uncertainty associated with the repeatability of the measurement was 0.01 S/m.

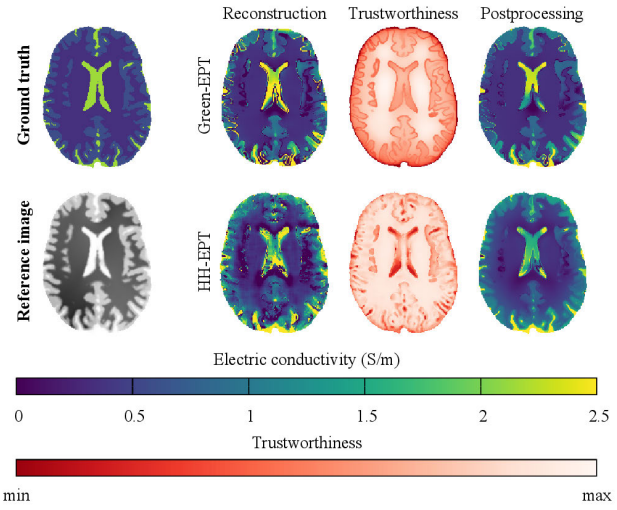

FIGURE 2. Transverse section of the analyzed digital brain, in the case of SNR = 150. The reconstructed conductivity, the corresponding voxel-wise trustworthiness, and the post-processed map are shown for Green-EPT and HH-EPT (complete versions). For both techniques, a cubic kernel ($L = 11$ voxels) has been used. The color scale is saturated between 0 and 2.5 S/m. Each map of trustworthiness spans from its own minimum (dark red) to maximum (white). The ground truth conductivity and the T1-weighted image used as a reference are also displayed.

The phantom was scanned at 123 MHz in a 3 T Siemens Prisma MR scanner (Siemens Healthineers, Germany), using the body coil as a transmitter. A 64-channel receiver head coil was used for SNR maximization and electronic noise minimization, with the vendor's specific correction (scan normalize) applied to obtain accurate phase measurements and remove non-uniform receiver coil profiles. Following standard MRI practice, calibration procedures were performed before data acquisition. Specifically, automated RF power calibration was executed by the system to ensure accurate flip angle delivery across the imaging volume. Moreover, volumetric shimming was applied within the field of view.

Phase maps were acquired using a multi-slice 2D balanced SSFP sequence, adopting a Cartesian sampling pattern (TR = 3.55 ms; TE = 1.78 ms; FA = 59°; FOV = 380 mm × 308 mm; Resolution = 1.5 mm × 1.5 mm; Slice thickness = 5 mm; Number of slices= 20). Phase maps from each channel were combined using a coil compression approach [35], which leads to a satisfactory homogeneity of the combined receive sensitivity.

The magnitude map of the acquired image was used both as a reference image and to remove the background voxels from the domain, using a thresholding of the magnitude map itself.

C. IN VIVO EXPERIMENTS

In vivo validations involved four healthy volunteers, who signed statements of informed consent and were recruited according to the protocol approved by the Institutional Review Boards. The same hardware adopted for the phantom experiment was used. The acquisition parameters were similar to those adopted for the phantom (TR = 4.36 ms; TE = 2.18 ms; FA = 25°; FOV = 250 mm × 250 mm; Resolution = 2 mm × 2 mm; Slice thickness = 2 mm; Number of slices = 32), but optimized to achieve optimal image quality. The reconstruction protocol was also similar.

IV. RESULTS

Relatively small kernels have been used, limiting the value of parameter N_T to a few units. Specifically, in reconstructions based on synthetic data and in vivo acquisitions, we set $N_T \leq 4$, whereas for the brain phantom we set $N_T \leq 2$.

The results obtained through a HH-EPT implementation that uses the reference image to weight the contributions to the fitting (Gaussian weight with 0.05 standard deviation) are also provided. For both techniques, the post-processing described in Sect. II-F has been adopted, setting D equal to 21 voxels. All HH-EPT results have been produced using EPTlib v0.4.0 (https://eptlib.github.io/) [36].

In all displayed maps, the color scale ranges from 0 to 2.5 S/m for conductivity, and from 0 to 130 for relative permittivity. For visualization purposes, values that are out of these ranges have been saturated to the nearest limit.

A. NUMERICAL SIMULATIONS

A first example of conductivity reconstruction, obtained at SNR = 150, is given in Fig. 2. On the left, the ground truth and the adopted reference image are provided. Both the Green-EPT and HH-EPT reconstructions have been obtained using a cubic kernel ($L_x = L_y = L_z = L = 11$ voxels), working with the complete (i.e., complex) version of the formulations. The figure shows the raw EPT reconstructions, the corresponding maps of trustworthiness, and the post-processed maps. In the maps of trustworthiness, the color ramp ranges from dark red (low trustworthiness) to white (high trustworthiness). We warn that, in their current form, the maps associated with the two EPT techniques are quantitative and self-consistent, but not fully comparable to each other in absolute terms. This limitation occurs because of the simplifying assumptions in the way in which the elements that influence trustworthiness have been modelled and accounted for. Thus, in this first attempt to quantify trustworthiness, the two maps shall not be compared.

The raw Green-EPT reconstruction has a good quality. With respect to the raw HH-EPT map, at a visual inspection it exhibits less spatial noise and a better definition of tissue boundaries. In the adopted HH-EPT implementation, the boundary error is virtually eliminated, because of the use of the reference image. In the map produced through Green-EPT, some boundary error is clearly visible (it manifests itself as a thin rim where the conductivity is higher, or lower, than the conductivity in the bulk of the adjacent tissues). However, the spatial extent of such an error is very limited. This provides first evidence of the fact that, when applied to heterogeneous kernels, Green-EPT manages the LHA in such a way to mitigate the corresponding model error.

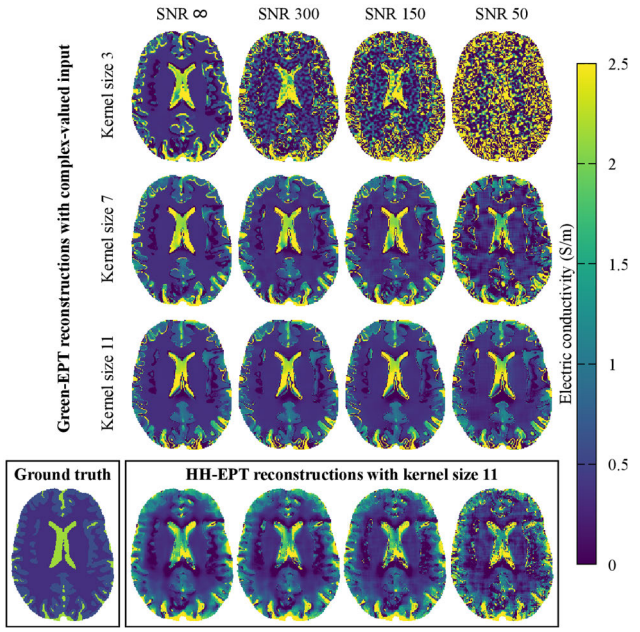

FIGURE 3. Raw conductivity reconstructions obtained through the complete version of Green-EPT at different SNR levels, changing the size of the kernel. The HH-EPT reconstruction, obtained using a cubic kernel ($L = 11$ voxels), is also displayed. The color scale of conductivity is saturated between 0 and 2.5 S/m.

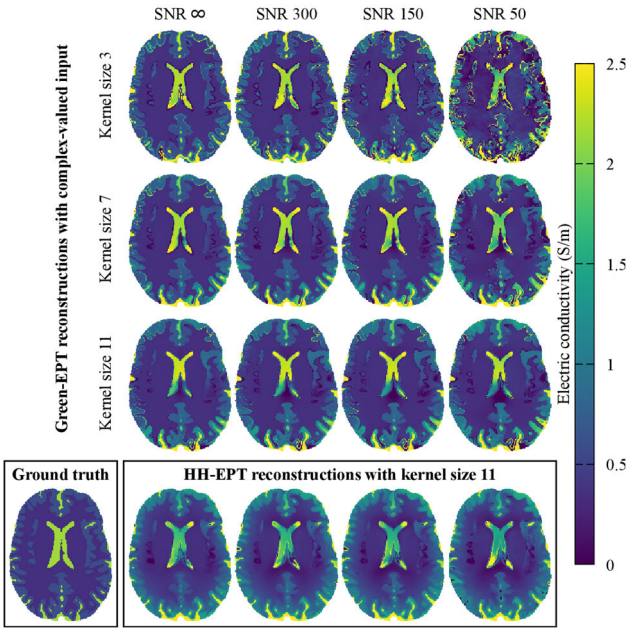

FIGURE 4. Post-processed conductivity maps obtained through the complete version of Green-EPT at different SNR levels, changing the size of the kernel. The HH-EPT reconstruction, obtained using a cubic kernel ($L = 11$ voxels), is also displayed. The color scale of conductivity is saturated between 0 and 2.5 S/m.

The map of trustworthiness of Green-EPT indicates that the reconstruction is more reliable in WM, whereas it becomes more uncertain in GM and in the cerebrospinal fluid (CSF). This reflects the geometrical complexity of the three tissues. The trustworthiness is also systematically lower along the interfaces. For HH-EPT, the situation is similar, but the map of trustworthiness is more heterogeneous and exhibits local minima in some anatomical details of small size. The application of the post-processing improves the Green-EPT reconstruction and produces a map that appears to be closer to the ground truth. In particular, even if some artifacts still exist (especially in CSF, and, to a lower extent, in GM), in the post-processed map all anatomical details are clearly visible, the tissues have a good level of homogeneity, and the rim at the border between different materials has been almost completely removed. Similarly, the post-processing effectively reduces the noise in the HH-EPT map, which is still more blurred than the Green-EPT map, anyway.

To investigate how the kernel size and the SNR level influence the results, the conductivity reconstructed by the complete version of Green-EPT is provided in Fig. 3 (raw map) and Fig. 4 (post-processed map), for different values of such parameters. Four SNR levels (50, 150, 300 and ∞) and three sizes of the cubic kernel (L equal to 3, 7, or 11 voxels) have been considered. The reconstruction obtained through HH-EPT, for the different SNR levels and keeping L equal to 11 voxels, is provided for comparison.

As expected, the best results are obtained in case of noiseless input. When the SNR decreases, a significant amount of noise affects the raw Green-EPT maps obtained using the smallest kernel. However, the results improve significantly as larger kernels are adopted. In particular, the case where $L = 11$ voxels produces maps that are almost completely stable across the investigated SNR levels. The quality of the raw HH-EPT maps depends on the SNR as well, but, using $L = 11$ voxels, the result is less robust than that produced through Green-EPT.

Maps almost identical to those given in Fig. 3 are obtained if the transmit phase is used instead of the transceive phase. Such maps, not reported for brevity, indicate that imperfections in the reconstruction under investigation should not be ascribed to the use of the transceive phase approximation.

When the raw Green-EPT maps are post-processed, the rim at the interface between different tissues tends to vanish and the noise is filtered substantially (even for small kernels). In particular, the kernel with $L = 11$ voxels produces a map that is highly stable with respect to the SNR levels, and in which the boundary error is no longer visible. HH-EPT benefits of the adopted post-processing too, producing maps where each tissue is more homogeneous, the interfaces are sharper, and the reconstruction is stable across the investigated SNR levels. These remarks also apply to Fig. 5, which shows post-processed sagittal and coronal maps obtained with $L = 11$ voxels and SNR $= 150$. The performance of the method is therefore stable along the longitudinal direction.

To evaluate the ability of Green-EPT to produce accurate quantitative results, Fig. 6 shows the statistical distribution of the conductivity reconstructed in the voxels belonging to the WM, GM and CSF compartments. The data refer to the case where $L = 11$ voxels, after the application of the

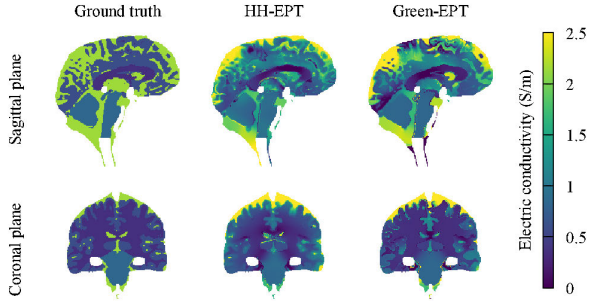

FIGURE 5. Post-processed conductivity maps obtained at SNR = 150 through the complete version of Green-EPT and HH-EPT, using a cubic kernel ($L = 11$ voxels), on sagittal and coronal sections. The ground truth is also displayed. The color scale of conductivity is saturated between 0 and 2.5 S/m.

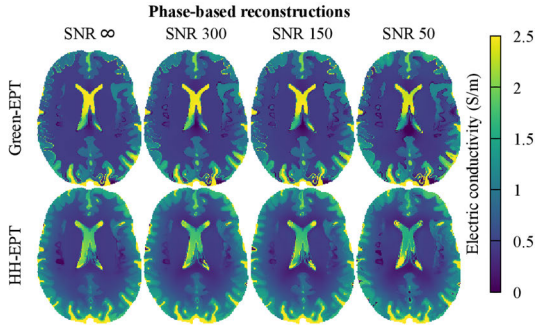

FIGURE 7. Post-processed conductivity maps obtained through the phase-based version of Green-EPT at different SNR levels, using a cubic kernel ($L = 11$ voxels). The corresponding HH-EPT reconstructions are also displayed. The color scale of conductivity is saturated between 0 and 2.5 S/m.

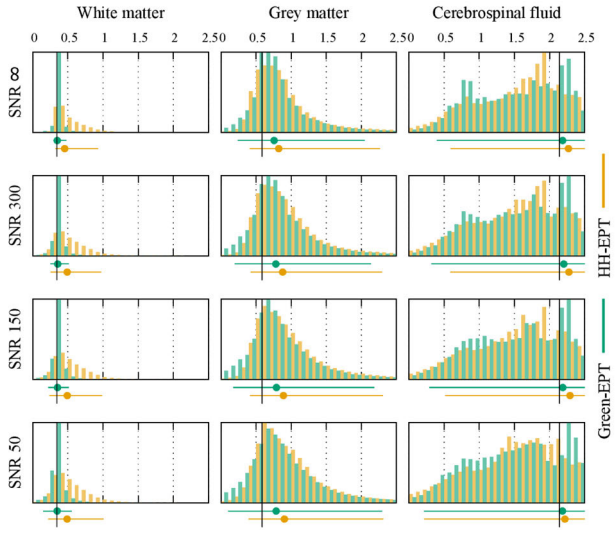

FIGURE 6. Distribution of the conductivity values (S/m) in WM, GM and CSF, for different SNR levels. Post-processed Green-EPT and HH-EPT results (cubic kernel with $L = 11$ voxels) are compared. Only values between 0 and 2.5 S/m are displayed. The median values and the 90 % coverage intervals are reported below each diagram. Vertical black lines indicate the ground truth. To improve visibility, each subplot has its own vertical axis.

post-processing. Analogous data produced through HH-EPT are also displayed. In WM, Green-EPT gives rise to an almost symmetric distribution, whose median value estimates the ground truth very well. The 90 % symmetric coverage interval (i.e., the range spanning from the 5^{th} to the 95^{th} percentile of the reconstructed conductivity values) is relatively small. The distribution produced by HH-EPT is more spread, less symmetric, and has a median value that tends to overestimate the true value. In GM, the distribution becomes wider, and the median tends to overestimate the ground truth. Also in this case, for HH-EPT the median value is more biased towards higher conductivity values. The width of the coverage intervals is similar for the two techniques. In CSF, the distribution is even broader and less regular. In this tissue, the median values of Green-EPT are in good agreement with the ground truth, whereas the medians of HH-EPT slightly overestimate it. For both techniques, in CSF a significant number of voxels has a reconstructed conductivity higher than 2.5 S/m. The upper bound of the coverage intervals exceeds this limit as well.

Qualitatively, these observations apply to all SNR levels, but the distributions get wider at the reduction of the SNR, while the median values keep stable. Histograms of the data before post-processing, not reported for brevity, show statistical distributions similar to those given in Fig. 6. However, without post-processing the coverage intervals are larger.

An example of conductivity reconstruction obtained through the phase-based version of Green-EPT, with $L = 11$ voxels, is given in Fig. 7, for different SNR levels (50, 150, 300 and ∞). In this case, only the post-processed maps are reported. The corresponding post-processed HH-EPT maps are also shown. At a visual inspection, the phase-based reconstructions of Green-EPT and HH-EPT appear almost identical to the corresponding reconstructions reported in Fig. 4. This confirms the opportunity to make use of the phase-based approximation in the case under investigation. The comparison between Figs. 4 and 7 puts in evidence only a slight systematic difference in terms of color tone (i.e., conductivity value). Precisely, the maps in Fig. 4 in general are slightly darker than the corresponding maps in Fig. 7.

The analysis of the results obtained working on synthetic input data concludes with an investigation of the reconstruction of relative permittivity. Fig. 8 compares the maps obtained through the complete version of Green-EPT and HH-EPT, for different SNR levels, using $L = 11$ voxels and applying the post-processing. For both techniques, the reconstruction of relative permittivity reveals to be more critical than the reconstruction of conductivity. For Green-EPT, a reasonable permittivity mapping is obtained in WM working on noiseless input data. In the other tissues, the image is significantly compromised. At the decrease of the SNR, some noise appears in WM. The situation is even worse for HH-EPT maps, where WM is affected by noise also with

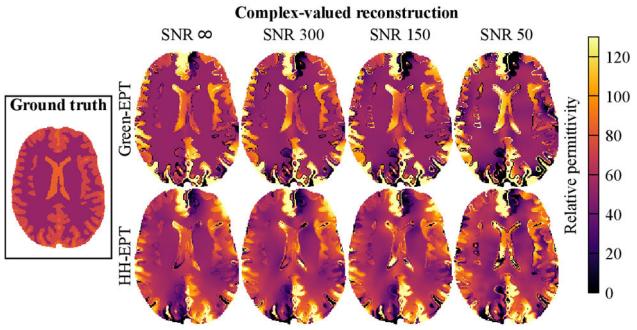

FIGURE 8. Post-processed relative permittivity maps obtained through the complex version of Green-EPT and HH-EPT, at different SNR levels, using a cubic kernel ($L = 11$ voxels). The ground truth is displayed on the left. The color scale is saturated between 0 and 130.

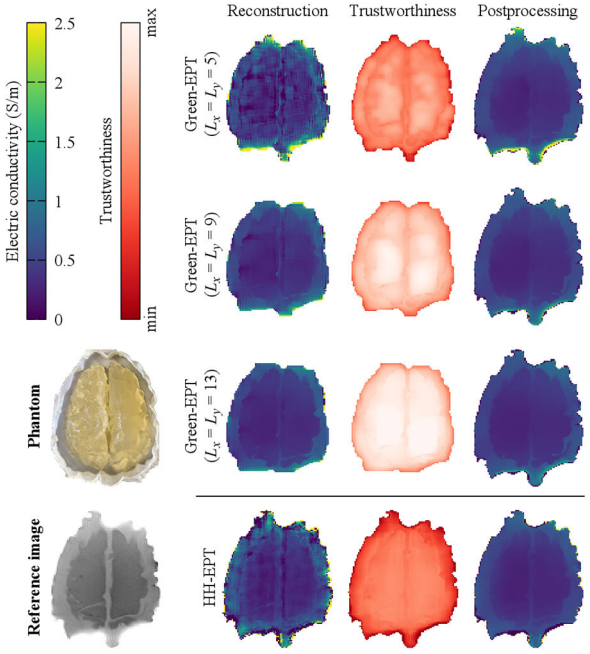

FIGURE 9. Results of the experiments performed on the brain phantom. On the left, a picture of the phantom (showing the WM compartment, placed within the external shell used to shape the GM) and the qualitative image used as a reference. On the right, for both Green-EPT and HH-EPT, the phase-based conductivity reconstruction, the corresponding voxel-wise trustworthiness, and the post-processed map. In HH-EPT, the kernel size is 11 × 11 × 7. In Green-EPT, $L_z = 3$ for all kernels. The color scale of conductivity is saturated between 0 and 2.5 S/m. The maps of trustworthiness span from their own minimum (dark red) to maximum (white).

the noiseless input, and the interfaces between tissues are always more blurred.

B. EXPERIMENTS ON A BRAIN PHANTOM

The results of the phase-based EPT reconstruction applied to the experimental data acquired on the brain phantom are summarized in Fig. 9, for both Green-EPT ($L_x = L_y = 5$, 9, or 13; $L_z = 3$) and HH-EPT ($L_x = L_y = 11$, $L_z = 7$). In our current implementation, Green-EPT skips the calculation of a kernel if a part of it falls outside the computational domain. Thus, taking into account the height of the phantom, the size of the kernel has been reduced in the longitudinal direction. As for the simulated input data, larger kernels filter the noise more effectively. This condition is well represented by the map of trustworthiness, which becomes brighter at the increase of the kernel size. Looking at the raw reconstruction obtained through the largest kernel, Green-EPT has produced a clean image, whereas the HH-EPT image is more noisy. The reliability of the Green-EPT reconstruction is higher in the inner, larger, WM compartment (where the map of trustworthiness is brighter). It gets worse in the outer GM layer, which is thinner, and reaches the minimum along the external border of the phantom. We remind that the maps of trustworthiness are produced following different procedures for the two techniques and therefore shall not be compared, quantitatively, to each other. The situation is similar for HH-EPT. Both techniques benefit from the application of the post-processing, which makes the EPT images more homogeneous within each compartment. This operation filters almost completely the noise of the raw HH-EPT reconstruction. For Green-EPT, the post-processing also has the effect of extending the imaged domain, recovering voxels that have been skipped in the raw Green-EPT reconstruction.

TABLE 1. EPT Conductivity reconstruction (S/m) in the phantom (median and 90 % coverage interval).

		Without post-processing	With post-processing
WM	Green-EPT	0.333 [0.251, 0.457]	0.319 [0.258, 0.435]
	HH-EPT	0.306 [0.196, 0.514]	0.301 [0.236, 0.426]
GM	Green-EPT	0.636 [0.348, 0.974]	0.555 [0.400, 0.826]
	HH-EPT	0.632 [0.218, 1.20]	0.553 [0.405, 0.727]

Reference values for the WM and GM tissue-mimicking materials are (0.29 ± 0.01) S/m and (0.59 ± 0.01) S/m, respectively.

To obtain a more quantitative evaluation of the conductivity provided by the two EPT techniques, Table 1 reports the median value and the lower and upper bounds of the 90 % coverage interval, calculated without and with the post-processing, in the two compartments of the phantom (for Green-EPT, the largest kernel was considered). To this end, the MRI magnitude map was used to segment the domain. Precisely, the contours of the image were enhanced with a Sobel filter, which allowed to identify five connected regions of WM. Each region was selected with a flood fill algorithm, starting from a seed point picked by hand. These regions were combined to provide the mask for the WM. Finally, the GM voxels were identified by removing the WM from the whole slice of interest and eroding the remaining region with a disk of 3 pixel radius.

A good level of consistency is observed between the two techniques. Looking at the raw data, in both compartments the width of the 90 % coverage interval is smaller for Green-EPT. In all cases, the effect of the post-processing

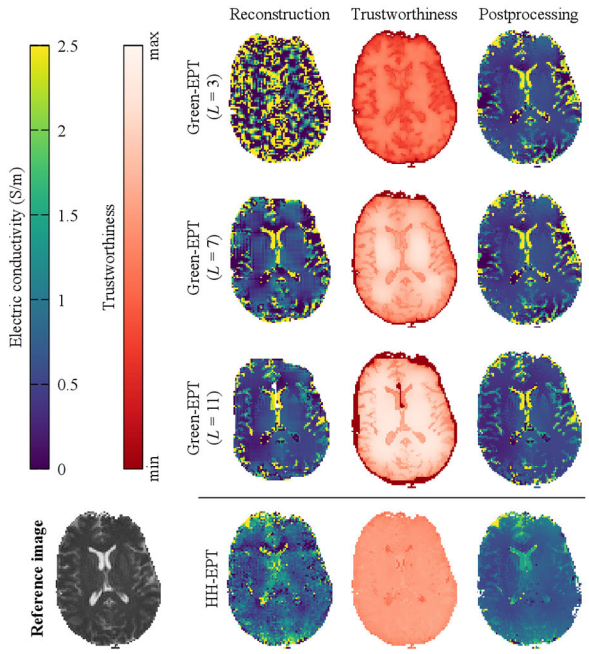

FIGURE 10. Effect of the kernel size on the phase-based conductivity reconstruction of the brain of human volunteer 1. The corresponding voxel-wise trustworthiness and the post-processed maps are also reported. The color scale of conductivity is saturated between 0 and 2.5 S/m. The maps of trustworthiness span from their own minimum (dark red) to maximum (white). The qualitative image used as a reference is reported on the left. In HH-EPT, $L = 11$ voxels.

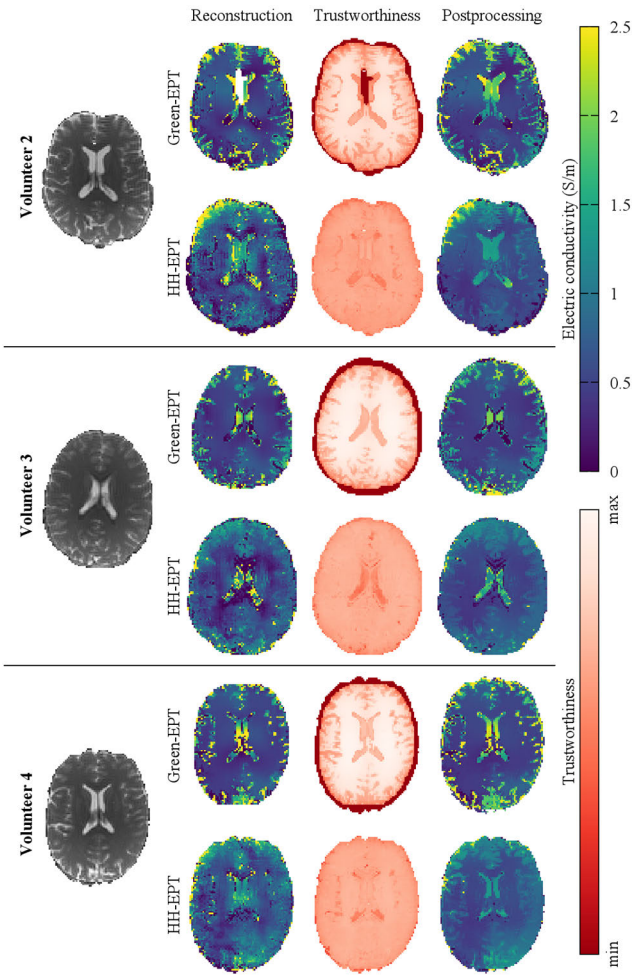

FIGURE 11. Results of the experiments performed on the brain of volunteers 2, 3 and 4. For both Green-EPT and HH-EPT, the phase-based conductivity reconstruction (kernel size: $L = 11$ voxels), the corresponding voxel-wise trustworthiness, and the post-processed map are reported. The color scale of conductivity is saturated between 0 and 2.5 S/m. The maps of trustworthiness span from their own minimum (dark red) to maximum (white). The qualitative images used as a reference are reported on the left.

is to bring the median values closer to the reference value, and to reduce the extent of the 90 % coverage intervals.

C. IN VIVO EXPERIMENTS

The results of the phase-based EPT applied to the data acquired on the four volunteers are summarized in Figs. 10 and 11, for both Green-EPT and HH-EPT. Specifically, Fig. 10 shows, for the first volunteer, the effect of the size of the kernel. Also in this case, at the increase of the kernel size the reconstructions produced by Green-EPT become less noisy. Parallel to this, the map of trustworthiness becomes brighter. Using the same kernel size ($L = 11$ voxels), raw Green-EPT results are less noisy than HH-EPT results, for all volunteers. For Green-EPT, the maps of trustworthiness exhibit a spatial pattern similar to that observed in Fig. 2 for synthetic data, with bright (i.e., more trustworthy) voxels in WM and darker voxels in GM and CSF. Minimum trustworthiness is obtained along the external border, where voxels participate at a relatively low number of kernels. With respect to Fig. 2, the external rim is thicker, because of the coarser resolution. For HH-EPT, the maps of trustworthiness are more homogeneous. A general improvement is obtained through the post-processing. The latter significantly reduces the noise in HH-EPT maps. Despite this, in HH-EPT the internal boundaries keep more blurred, whereas Green-EPT maps are sharper.

V. DISCUSSION AND CONCLUSIONS

A. DISCUSSION OF THE NUMERICAL SIMULATIONS

Raw reconstructions performed on synthetic data show that, in terms of noise, Green-EPT performs on par, and often even better, than HH-EPT. It must be remarked that Green-EPT makes use of an extra layer of voxels around the kernel to perform the calculation. Nevertheless, raw Green-EPT maps obtained with $L = 7$ voxels already exhibit lower noise than raw HH-EPT maps obtained with $L = 11$ voxels.

A careful inspection of the maps obtained with noiseless input reveals how Green-EPT manages boundary errors. In the bulk of the tissues, the results obtained with the smallest kernel are close to the ground truth. However, some boundary error is visible at tissue interfaces. With larger kernels (fundamental in the presence of noise) the regularization due to the overdetermined system of equations almost completely removes the boundary errors from the maps. This

occurs at the cost of a mild reduction of accuracy in the tissues. We ascribe this drawback to two opposite mechanisms. In larger kernels, the regularization is stronger, but, in general, it has to cope with a higher number of interfaces, where the LHA fails. Currently, we identify this feature as the main limitation of the method.

Considering the good results obtained by Green-EPT with $L = 11$ voxels, a further increase of the kernel size has not been pursued. Indeed, it would have implied a heavier computational burden for each kernel, unjustified in the light of the satisfactory results. Moreover, we notice that an increase of L makes the segmentation within the kernel more difficult, possibly requiring more sophisticated segmentation algorithms. The choice to keep the kernel quite small is even more justified if the post-processing is considered as an integral part of the EPT reconstruction. Indeed, as already observed, the adopted post-processing performs an effective filtering of residual boundary errors and spatial noise, even for quite small kernels.

Because of its practicality, the phase-based version of the formulation deserves a specific comment. As illustrated in Sect. IV-A, the phase-based approximation has produced a deviation of the conductivity values with respect to those obtained using the complete version of the method. This is in line with a widely reported tendency of phase-based EPT formulations to produce quantitative values that are biased (overestimated, typically) with respect to the results obtained working on complex input data [1], [2], [36], [38]. Considering the median values observed in Fig. 6 (which, in general, tend to be slightly higher than the ground truth), the phase-based approximation has induced a mild loss of accuracy in the estimate of the conductivity.

As regards relative permittivity, the outcomes illustrated in Fig. 8 are in line with previous studies that have put in evidence how this reconstruction is inherently more challenging [39]. Hence, they do not represent a specific failure of Green-EPT.

B. DISCUSSION OF THE EXPERIMENTS

The discussion of the experiments performed on the brain phantom and on the human volunteers cannot benefit of the availability of the ground truth. Hence, indirect evidence of the quality of the results must be looked for.

For the brain phantom, a good consistency has been observed between Green-EPT and HH-EPT. The consistency also extends to the reference values obtained through the characterization of the samples of the tissue-mimicking materials. The latter shall not be considered as ''true values'', anyway, because they are in turn affected by uncertainty and because the dielectric properties of the materials might have undergone some change during the preparation of the phantom. Interestingly, the median values in the raw EPT reconstructions are higher than the reference values. This might be due to the phase-based approximation. In all cases, the post-processing tends to reconcile the reconstructions and the reference values. For in vivo experiments, neither a ground truth, nor subject-specific reference values are available. However, a reasonable level of agreement is found between the reconstructed conductivities and those found in the literature [31]. Together with the good visual appearance of the EPT maps, all these elements suggest that a good quantification of the conductivity has been obtained.

Since the brain phantom does not reproduce the features of any of the volunteers' brains, a rigorous quantitative comparison between the results of the two experiments cannot be performed. The same is true for the synthetic data, which were obtained from a virtual anatomical model. Nevertheless, some cross comparisons between the three targets of this study can be performed, shedding light on some subtle aspects of the EPT reconstruction. In general, the pipeline for the acquisition of experimental data is more complex than the simulated counterpart, and therefore it is more prone to elements that can generate artifacts and compromise the quality of the input data. On the other hand, the reconstructions performed on experimental data were carried out using a slightly coarser resolution, which tends to produce some noise suppression. We note that the geometry of the phantom is simpler than the geometry analyzed in both the simulations and the in vivo experiments (which are more similar to each other, from this viewpoint). Furthermore, some diffusion might have smoothed the transition of the conductivity across the two compartments of the phantom. These features can explain the almost complete absence of outliers localized at the interface of the phantom compartments, as well as the narrow coverage intervals reported in Table 1 (which result to be relatively short, for both Green-EPT and HH-EPT, with respect to those reported in Fig. 6 for the simulated data, for all considered SNR values). Moreover, the phantom has the advantage of being perfectly at rest during the acquisition. Hence, it does not suffer from any motion (including the motion of internal fluids, like blood and CSF) which may affect in vivo experiments. For the latter, coverage intervals were not calculated (this would have required a segmentation of the entire brain of the volunteers; an operation that in turn introduces some uncertainty). However, at a visual inspection, the spatial dispersion observed in vivo seems to be reasonably consistent with the dispersion observed for the simulations.

C. FURTHER DISCUSSIONS AND CONCLUDING REMARKS

The originality of Green-EPT resides in two key steps of its formulation. The first is the idea to make use of the Green function for Poisson problems, which does not depend on the dielectric properties of the medium. We notice that, in [4], a ''Poisson-based conductivity mapping'', based on [40] and [41], is mentioned. Such approaches are deeply different from Green-EPT and should not be mistaken for it. The second element of originality is the idea to leave the kernel free to be heterogeneous. Combined with the possibility to exploit a reference image to group the unknowns, this has the effect to mitigate the boundary errors.

Green-EPT can be classified as a direct integral method and, in the proposed form, it is a local technique. This is an unusual feature in the EPT world. Another example of a direct, integral, local method can be found in [42], where the integral version of HH-EPT, originally presented in [37], is analyzed. However, in that integral approach, the kernel is still considered homogeneous, like in the differential HH-EPT. Hence, such an approach suffers the boundary errors, unless it is applied in combination with a reference image, which allows performing the reconstruction in a presumably homogeneous region. Rather, the integral version of HH-EPT was conceived to make HH-EPT more robust with respect to noise. This was achieved by manipulating the differential form of HH-EPT through the first of Green's identities, obtaining a formulation involving first order, instead of second order, spatial derivatives. We point out that, making reference to the original work by George Green ("An Essay on the Application of Mathematical Analysis to the Theories of Electricity and Magnetism", 1828), our equation (10) corresponds to his third integral identity, which gives rise to the peculiar approach presented in this paper.

In principle, Green-EPT could be applied to the whole domain at once, becoming a global method. In this case, the Green function would allow dealing with the proper spatial distribution of the field, without binding it to arbitrary behaviors (e.g., the quadratic distribution typically adopted in HH-EPT) that represent local approximations (cf. Appendix A). This implementation would require much more computational power. Hence, at the moment it has not been tested yet.

In terms of computational efficiency, currently Green-EPT has been implemented in MATLAB, to provide a proof of concept, without special care to optimization. On the contrary, our HH-EPT [36], implemented in C++, has a higher level of optimization and can exploit parallel computing. Comparing the phase-based versions of the two techniques on a single CPU thread, at the present stage HH-EPT is about 25 times faster than Green-EPT. Considering the wide margin of optimization, we conjecture that future implementations of Green-EPT will reach similar speeds as HH-EPT. The complex version of Green-EPT is about four times slower than the phase-based version. This occurs because the former solves a complex matrix, whereas the latter solves a real matrix (in HH-EPT the speed keeps almost the same, because the matrix associated with the quadratic fitting is real in both cases).

The map of trustworthiness is a remarkable collateral result of the proposed research, which provides a visual indication of the reliability of the conductivity values assigned to each voxel. The map must be interpreted ponderingly: brighter voxels have a higher probability to have a conductivity value close to the ground truth, whereas, in darker voxels, this probability is lower. At first sight, in the reported maps, T seems to be inversely correlated with σ (i.e., higher T in WM). Actually, this occurs because of the geometrical features of WM, which allow a more effective mitigation of the drawback associated with the LHA. Besides its direct use to evaluate the reliability, the map of trustworthiness turns out to be a useful tool to post-process the raw EPT maps, obtaining a "reliability-informed" post-processing. As shown, this type of filter not only improves the quality of the Green-EPT maps, but it is even more effective in refining HH-EPT reconstructions.

In the light of the obtained promising results, future works will focus on some technical improvements. Specifically, the possibility to shape the kernel to work along the external boundary of the domain will be considered. This will allow filling the entire domain already at the stage of the raw reconstruction. Moreover, since a residual effect of the LHA affects some reconstructions (precisely, a mild bias in the bulk of the tissues, identified as the main drawback of the method), the possibility to modify the formulation and completely avoid the LHA will be pursued. Finally, the concept of trustworthiness will be elaborated further. Specifically, a strategy to estimate the level of correlation between the conductivity values calculated in a given voxel for different kernels will be developed, taking into account the spatial overlap between such kernels. This will lead to T maps that can resemble a more rigorous uncertainty evaluation [27].

From the viewpoint of the application, the possibility to characterize pathological anomalies will be investigated. This will require a dedicated analysis, where the size, the contrast and the position of the anomalies within anatomical structures will be considered.

APPENDIX A
ANALYTICAL EQUIVALENCE BETWEEN GREEN-EPT AND HH-EPT IN HOMOGENEOUS REGIONS

If Green-EPT is applied to a homogeneous region, and the sampled B_1^+ data are preliminarily fitted (as usually done for HH-EPT), the problem can be written in a closed form, which turns out to be equivalent to the one obtained for HH-EPT. To show this, we refer to a point P (the barycenter of a voxel) which acts as the origin of a Cartesian reference frame, where the field distribution is approximated through a quadratic fitting

$$\begin{aligned} B_1^+(x,y,z) = {} & c_1 + c_2 x + c_3 y + c_4 z + c_5 x^2 \\ & + c_6 y^2 + c_7 z^2 + c_8 xy + c_9 xz + c_{10} yz, \end{aligned} \tag{A1}$$

which implies $B_1^+(P) = c_1$. If we rewrite (A1) for a spherical reference frame (with colatitude θ and longitude ϕ) centered in P, the integrals in (10) can be calculated analytically. Most of the coefficients of the fitting do not contribute to the integrals; the only non-null contributions lead to:

$$\begin{aligned} & \oint_S B_1^+ (\nabla \Psi \cdot \boldsymbol{n}) ds \\ & = \int_0^{2\pi} \int_0^{\pi} B_1^+ \left[\frac{d}{dr} \left(\frac{1}{4\pi r} \right) \right]_{r=R} R^2 \sin\theta d\theta d\phi \\ & = -\frac{1}{4\pi} \int_0^{2\pi} \int_0^{\pi} B_1^+ \sin\theta d\theta d\phi \end{aligned}$$

$$= -\left(c_1 + R^2 \frac{c_5 + c_6 + c_7}{3}\right) \tag{A2}$$

$$\oint_S \Psi \left(\nabla B_1^+ \cdot \boldsymbol{n}\right) ds$$
$$= \int_0^{2\pi} \int_0^{\pi} \left[\frac{1}{4\pi r} \frac{dB_1^+}{dr}\right]_{r=R} R^2 \sin\theta d\theta d\phi$$
$$= \frac{R}{4\pi} \int_0^{2\pi} \int_0^{\pi} \left[\frac{dB_1^+}{dr}\right]_{r=R} \sin\theta d\theta d\phi$$
$$= \frac{2}{3} R^2 \left(c_5 + c_6 + c_7\right) \tag{A3}$$

$$\int_V B_1^+ \Psi dv$$
$$= \int_0^{2\pi} \int_0^{\pi} \int_0^{R} \left(\frac{B_1^+}{4\pi r}\right) r^2 \sin\theta dr d\theta d\phi$$
$$= \frac{R^2}{2} \left(c_1 + R^2 \frac{c_5 + c_6 + c_7}{6}\right) \tag{A4}$$

where R is the radius of the sphere with volume V and surface S, centered in P.

Once the integrals in (A2)-(A4) are substituted into (10), taking the limit for $R \to 0$ (i.e., shrinking the sphere around point P), the dielectric properties can be calculated as

$$\left(\varepsilon - \mathrm{j}\frac{\sigma}{\omega}\right) = -\frac{2}{\omega^2 \mu_0} \frac{c_5 + c_6 + c_7}{c_1} \tag{A5}$$

which is the same formula commonly adopted in HH-EPT. We notice that the limit for $R \to 0$ is required because, strictly speaking, the quadratic fitting adopted in (A1) is only a local approximation of the B_1^+ distribution. Such a fitting is an essential ingredient in HH-EPT, whereas it is not used in Green-EPT. The latter has therefore a wider generality, from the analytic viewpoint, because it makes use of the Green function to take into account the actual "shape" of the field.

APPENDIX B
ALTERNATIVE FORMULATION OF GREEN-EPT

The proposed Green-EPT technique has been developed looking at (5) as a Poisson equation. This "trick" produces a substantial simplification of the formulation, because of the use of a static Green function that does not depend on the properties of the medium. However, nothing prevents from using Green's integral identity to handle (5) as a complex Helmholtz equation, as it actually is. In this case, for a generic point P within a region Ω surrounded by a closed surface $\partial\Omega$, the use of Green's identity leads to an integral representation in the form [26]

$$B_1^+(P) = \oint_{\partial\Omega} \left(\widetilde{\Psi} \nabla B_1^+ \cdot \boldsymbol{n} - B_1^+ \nabla \widetilde{\Psi} \cdot \boldsymbol{n}\right) ds. \tag{B1}$$

The latter equation seems to be simpler than (9), because of the absence of any volume integral. Actually, it requires the use of the Green function for three-dimensional Helmholtz problems, i.e., $\widetilde{\Psi} = e^{-\mathrm{j}\gamma r}/(4\pi r)$, where $\gamma = \omega(\varepsilon - \mathrm{j}\sigma/\omega)^{-1/2}$ is the propagation factor. Such a Green function involves the dielectric properties; hence, the use of (B1) is restricted to homogeneous regions only. Moreover, the presence of the dielectric properties within the Green function makes the EPT problem based on (B1) less straightforward to solve with respect to the Green-EPT based on (11). Finally, we notice that the use of a static Green function is the most natural choice when handling the approximated (phase-based) problem described through (7), which is really a Poisson equation.

REFERENCES

[1] U. Katscher, D.-H. Kim, and J. K. Seo, "Recent progress and future challenges in MR electric properties tomography," *Comput. Math. Methods Med.*, vol. 2013, Mar. 2013, Art. no. 546562.
[2] U. Katscher and C. A. T. van den Berg, "Electric properties tomography: Biochemical, physical and technical background, evaluation and clinical applications," *NMR Biomed.*, vol. 30, no. 8, p. e3729, Aug. 2017.
[3] J. Liu, Y. Wang, U. Katscher, and B. He, "Electrical properties tomography based on B_1 maps in MRI: Principles, applications, and challenges," *IEEE Trans. Biomed. Eng.*, vol. 64, no. 11, pp. 2515–2530, Nov. 2017.
[4] R. Leijsen, W. Brink, C. van den Berg, A. Webb, and R. Remis, "Electrical properties tomography: A methodological review," *Diagnostics*, vol. 11, no. 2, p. 176, Jan. 2021.
[5] S.-Y. Kim, J. Shin, D.-H. Kim, M. J. Kim, E.-K. Kim, H. J. Moon, and J. H. Yoon, "Correlation between conductivity and prognostic factors in invasive breast cancer using magnetic resonance electric properties tomography (MREPT)," *Eur. Radiol.*, vol. 26, no. 7, pp. 2317–2326, Jul. 2016.
[6] K. K. Tha, U. Katscher, S. Yamaguchi, C. Stehning, S. Terasaka, N. Fujima, K. Kudo, K. Kazumata, T. Yamamoto, M. Van Cauteren, and H. Shirato, "Noninvasive electrical conductivity measurement by MRI: A test of its validity and the electrical conductivity characteristics of glioma," *Eur. Radiol.*, vol. 28, no. 1, pp. 348–355, Jan. 2018.
[7] N. Mori, K. Tsuchiya, D. Sheth, S. Mugikura, K. Takase, U. Katscher, and H. Abe, "Diagnostic value of electric properties tomography (EPT) for differentiating benign from malignant breast lesions: Comparison with standard dynamic contrast-enhanced MRI," *Eur. Radiol.*, vol. 29, no. 4, pp. 1778–1786, Apr. 2019.
[8] U. Jensen-Kondering, L. Shu, R. Böhm, O. Jansen, and U. Katscher, "In-vivo pilot study at 3 tesla: Feasibility of electric properties tomography in a rat model of stroke," *Phys. Med.*, vol. 9, Jun. 2020, Art. no. 100024.
[9] K. K. Tha, Y. Kikuchi, K. Ishizaka, T. Kamiyama, M. Yoneyama, and U. Katscher, "Higher electrical conductivity of liver parenchyma in fibrotic patients: Noninvasive assessment by electric properties tomography," *J. Magn. Reson. Imag.*, vol. 54, no. 5, pp. 1689–1691, Nov. 2021.
[10] S. Park, S. M. Jung, M. B. Lee, H. Y. Rhee, C.-W. Ryu, A. R. Cho, O. I. Kwon, and G.-H. Jahng, "Application of high-frequency conductivity map using MRI to evaluate it in the brain of Alzheimer's disease patients," *Frontiers Neurol.*, vol. 13, May 2022, Art. no. 872878.
[11] E. Balidemaj, H. P. Kok, G. Schooneveldt, A. L. H. M. W. van Lier, R. F. Remis, L. J. A. Stalpers, H. Westerveld, A. J. Nederveen, C. A. T. van den Berg, and J. Crezee, "Hyperthermia treatment planning for cervical cancer patients based on electrical conductivity tissue properties acquiredin vivowith EPT at 3 T MRI," *Int. J. Hyperthermia*, vol. 32, no. 5, pp. 558–568, Jul. 2016.
[12] F. Liporace and M. Cavagnaro, "Development of mr-based procedures for the implementation of patient-specific dielectric models for clinical use," *J. Mech. Med. Biol.*, vol. 23, no. 6, May 2023, Art. no. 2340031.
[13] U. Katscher, T. Voigt, C. Findeklee, P. Vernickel, K. Nehrke, and O. DÖssel, "Determination of electric conductivity and local SAR via B1 mapping," *IEEE Trans. Med. Imag.*, vol. 28, no. 9, pp. 1365–1374, Sep. 2009.
[14] X. Zhang, S. Schmitter, P. F. Van de Moortele, J. Liu, and B. He, "From complex B1 mapping to local SAR estimation for human brain MR imaging using multi-channel transceiver coil at 7T," *IEEE Trans. Med. Imag.*, vol. 32, no. 6, pp. 1058–1067, Jun. 2013.
[15] J. A. Martinez, A. Arduino, O. Bottauscio, and L. Zilberti, "Evaluation and correction of B_1^+-based brain subject-specific SAR maps using electrical properties tomography," *IEEE J. Electromagn., RF Microw. Med. Biol.*, vol. 7, no. 2, pp. 420–435, Jun. 2023.

[16] F. S. Hafalir, O. F. Oran, N. Gurler, and Y. Z. Ider, "Convection-reaction equation based magnetic resonance electrical properties tomography (cr-MREPT)," *IEEE Trans. Med. Imag.*, vol. 33, no. 3, pp. 777–793, Mar. 2014.

[17] N. Eda, M. Fushimi, K. Hasegawa, and T. Nara, "A method for electrical property tomography based on a three-dimensional integral representation of the electric field," *IEEE Trans. Med. Imag.*, vol. 41, no. 6, pp. 1400–1409, Jun. 2022.

[18] E. Michel, D. Hernandez, and S. Y. Lee, "Electrical conductivity and permittivity maps of brain tissues derived from water content based on T1-weighted acquisition," *Magn. Reson. Med.*, vol. 77, no. 3, pp. 1094–1103, Mar. 2017.

[19] S. Mandija, E. F. Meliadò, N. R. F. Huttinga, P. R. Luijten, and C. A. T. van den Berg, "Opening a new window on MR-based electrical properties tomography with deep learning," *Sci. Rep.*, vol. 9, no. 1, Jun. 2019, Art. no. 8895.

[20] S.-K. Lee, S. Bulumulla, and I. Hancu, "Theoretical investigation of random noise-limited signal-to-noise ratio in MR-based electrical properties tomography," *IEEE Trans. Med. Imag.*, vol. 34, no. 11, pp. 2220–2232, Nov. 2015.

[21] J. K. Seo, M.-O. Kim, J. Lee, N. Choi, E. J. Woo, H. J. Kim, O. I. Kwon, and D.-H. Kim, "Error analysis of nonconstant admittivity for MR-based electric property imaging," *IEEE Trans. Med. Imag.*, vol. 31, no. 2, pp. 430–437, Feb. 2012.

[22] S. Mandija, A. Sbrizzi, U. Katscher, P. R. Luijten, and C. A. T. van den Berg, "Error analysis of helmholtz-based MR-electrical properties tomography," *Magn. Reson. Med.*, vol. 80, no. 1, pp. 90–100, Jul. 2018.

[23] E. Balidemaj, C. A. T. van den Berg, J. Trinks, A. L. H. M. W. van Lier, A. J. Nederveen, L. J. A. Stalpers, H. Crezee, and R. F. Remis, "CSI-EPT: A contrast source inversion approach for improved MRI-based electric properties tomography," *IEEE Trans. Med. Imag.*, vol. 34, no. 9, pp. 1788–1796, Sep. 2015.

[24] L. Huang, F. Schweser, K. Herrmann, M. Krämer, A. Deistung, and JR Reichenbach, "A Monte Carlo method for overcoming the edge artifacts in MRI-based electrical conductivity mapping," in *Proc. Int. Soc. Mag. Reson. Med. (ISMRM)*, vol. 2014, p. 3190.

[25] J. Lee, J. Shin, and D.-H. Kim, "MR-based conductivity imaging using multiple receiver coils," *Magn. Reson. Med.*, vol. 76, no. 2, pp. 530–539, Aug. 2016.

[26] P. Morse and H. Feshbach, *Methods of Theoretical Physics*. New York, NY, USA: McGraw-Hill, 1953, pp. 804–891.

[27] *Evaluation of Measurement Data—Guide To the Expression of Uncertainty in Measurement*, 1st ed., Joint Committee for Guides Metrology (JCGM), Paris, France, 2008.

[28] A. Arduino and L. Zilberti, "Metrological contributions to magnetic resonance-based electric properties tomography," presented at the 17th Eur. Conf. Antennas Propag. (EuCAP), Florence, Italy, Mar. 2023. [Online]. Available: https://ieeexplore.ieee.org/document/10132952

[29] *Sim4Life*. Accessed: Feb. 26, 2025. [Online]. Available: https://zmt.swiss/sim4life/

[30] M.-C. Gosselin, E. Neufeld, H. Moser, E. Huber, S. Farcito, L. Gerber, M. Jedensjö, I. Hilber, F. D. Gennaro, B. Lloyd, E. Cherubini, D. Szczerba, W. Kainz, and N. Kuster, "Development of a new generation of high-resolution anatomical models for medical device evaluation: The virtual population 3.0," *Phys. Med. Biol.*, vol. 59, no. 18, pp. 5287–5303, Sep. 2014.

[31] P. A. Hasgall, E. Neufeld, M. C. Gosselin, A. Klingenböck, N. Kuster, N. Kuster, P. Hasgall, and M. Gosselin, "IT'IS database for thermal and electromagnetic parameters of biological tissues," Version 4.1, IT'IS Foundation, Zurich, Switzerland, Tech. Rep., Feb. 2022, doi: 10.13099/VIP21000-04-1.

[32] W. P. Segars, J. Bond, J. Frush, S. Hon, C. Eckersley, C. H. Williams, J. Feng, D. J. Tward, J. T. Ratnanather, M. I. Miller, D. Frush, and E. Samei, "Population of anatomically variable 4D XCAT adult phantoms for imaging research and optimization: Population of anatomically variable 4D XCAT adult phantoms," *Med. Phys.*, vol. 40, no. 4, Apr. 2013, Art. no. 043701.

[33] C. Ianniello, J. A. de Zwart, Q. Duan, C. M. Deniz, L. Alon, J. Lee, R. Lattanzi, and R. Brown, "Synthesized tissue-equivalent dielectric phantoms using salt and polyvinylpyrrolidone solutions," *Magn. Reson. Med.*, vol. 80, no. 1, pp. 413–419, Jul. 2018.

[34] J. Martinez, A. Troia, A. Arduino, K. Moulin, U. Zanovello, O. Bottauscio, and L. Zilberti, "Imaging-based subject-specific SAR maps using B1-mapping and electrical properties tomography in a heterogenous brain phantom," in *Proc. ISMRM Annu. Meeting*, 2023, p. 5229.

[35] T. Zhang, J. M. Pauly, S. S. Vasanawala, and M. Lustig, "Coil compression for accelerated imaging with Cartesian sampling," *Magn. Reson. Med.*, vol. 69, no. 2, pp. 571–582, Feb. 2013.

[36] A. Arduino, "EPTlib: An open-source extensible collection of electric properties tomography techniques," *Appl. Sci.*, vol. 11, no. 7, p. 3237, Apr. 2021.

[37] T. Voigt, U. Katscher, and O. Doessel, "Quantitative conductivity and permittivity imaging of the human brain using electric properties tomography: In vivo electric properties tomography," *Magn. Reson. Med.*, vol. 66, no. 2, pp. 456–466, Aug. 2011.

[38] A. Arduino, F. Pennecchi, U. Katscher, M. Cox, and L. Zilberti, "Repeatability and reproducibility uncertainty in magnetic resonance-based electric properties tomography of a homogeneous phantom," *Tomography*, vol. 9, no. 1, pp. 420–435, Feb. 2023.

[39] S. Gavazzi, C. A. T. van den Berg, A. Sbrizzi, H. P. Kok, L. J. A. Stalpers, J. J. W. Lagendijk, H. Crezee, and A. L. H. M. W. van Lier, "Accuracy and precision of electrical permittivity mapping at 3T: The impact of three mapping techniques," *Magn. Reson. Med.*, vol. 81, no. 6, pp. 3628–3642, Jun. 2019.

[40] A. Borsic, I. Perreard, A. Mahara, and R. J. Halter, "An inverse problems approach to MR-EPT image reconstruction," *IEEE Trans. Med. Imag.*, vol. 35, no. 1, pp. 244–256, Jan. 2016.

[41] K. M. Ropella and D. C. Noll, "A regularized, model-based approach to phase-based conductivity mapping using MRI," *Magn. Reson. Med.*, vol. 78, no. 5, pp. 2011–2021, Nov. 2017.

[42] A. Karsa and K. Shmueli, "New approaches for simultaneous noise suppression and edge preservation to achieve accurate quantitative conductivity mapping in noisy images," in *Proc. Int. Soc. Mag. Reson. Med. (ISMRM)*, vol. 29, 2021, p. 3774.

LUCA ZILBERTI was born in Vercelli, Italy, in 1982. He received the B.Sc., M.Sc., and Ph.D. degrees in electrical engineering from Politecnico di Torino, Turin, Italy, in 2004, 2006, and 2010, respectively. In 2010, he joined the Istituto Nazionale di Ricerca Metrologica, Turin, where he is currently a Senior Researcher. In 2022, he got the national qualification as a Full Professor of electrical engineering. He serves on the governing committee of the study group on MR Safety of the International Society for Magnetic Resonance in Medicine (ISMRM). He participated in several research projects and coordinated the European EMPIR Project 18HLT05 "Quantitative MR-based imaging of physical biomarkers," (2019–2022). His research interests include the development of computational methods for electromagnetic dosimetry and biomedical applications of electromagnetic fields. In 2016, he was a recipient of the Young Scientist Award from the International Commission on Non-Ionizing Radiation Protection (ICNIRP).

ALESSANDRO ARDUINO received the B.Sc. degree in mathematics for engineering sciences, the M.Sc. degree in mathematical engineering, and the Ph.D. degree in electrical, electronics, and communications engineering from the Politecnico di Torino, Turin, Italy, in 2012, 2014, and 2018, respectively. Since 2018, he has been with the Istituto Nazionale di Ricerca Metrologica, Turin, Italy. He is the Maintainer of EPTlib, an open-source C++ library of electric properties tomography methods. His research interests include mathematical and numerical modeling of electromagnetism applied to biomedical engineering and inverse problems.

UMBERTO ZANOVELLO was born in Turin, Italy, in 1988. He received the B.S. and M.S. degrees in electrical engineering and the Ph.D. degree in electrical, electronics and communications engineering from Politecnico di Torino, Turin, in 2011, 2014, and 2019, respectively. He has been a permanent Researcher with the Istituto Nazionale di Ricerca Metrologica (INRiM), Turin, since 2021. His research interests include MRI safety and hardware design, with a particular focus on radiofrequency coils.

JESSICA A. MARTINEZ received the B.S. degree in physics from the University of the Américas Puebla, Mexico, in 2012, and the Ph.D. degree in bioengineering from the University of California at Los Angeles, USA, in 2019. She was a Postdoctoral Researcher with the Istituto Nazionale di Ricerca Metrologica, Turin, Italy, from 2021 to 2023. She is currently a Postdoctoral Associate with the University of Colorado, Boulder, CO, USA, and the National Institute of Standards and Technology (NIST). Her research interests include MRI safety, quantitative MRI, electromagnetic tissue properties, and electromagnetic dosimetry focused on biomedical and clinical applications. She was awarded the International Society for Magnetic Resonance in Medicine's 2023 Junior Research Fellow Award.

KEVIN MOULIN received the B.S. and M.S. degrees in biomedical engineering from the Polytech Engineering School, Lyon, France, and the Ph.D. degree from the University of Lyon under the supervision of Dr. Magalie Viallon and Pr. Pierre Croisille. He then completed postdoctoral training with UCLA, Stanford University, and the University of Lyon. He recently joined the Boston Children's Hospital Faculty as an Instructor, in October 2022. His research activities cover the development and translational application of advanced MRI acquisitions and reconstruction techniques for chest, abdominal, and cardiovascular applications. He has worked in the emergent field of cardiac diffusion imaging in which he developed robust free-breathing and cardiac motion-compensation techniques. For this work, he was awarded an American Heart Association (AHA) Postdoctoral Fellowship, in 2020.

ADRIANO TROIA received the Ph.D. degree in material science and technology from Politecnico di Torino, Turin, Italy, in 2006. He is currently a Researcher with the Istituto Nazionale di Ricerca Metrologica (INRiM), Turin. He works on the chemical synthesis of nanocarriers and phantoms for therapeutic and diagnostic applications of MRI and ultrasound. He is the author of more than 50 scientific articles and the WP leader for national and European projects.

ORIANO BOTTAUSCIO was born in Turin, Italy, in 1961. He received the M.Sc. degree in electrical engineering from Politecnico di Torino, in 1985. In 1987, he joined the Istituto Nazionale di Ricerca Metrologica (INRiM), formerly Istituto Elettrotecnico Nazionale Galileo Ferraris, and got the level of the Research Director, in 2012. In the same year, he received the qualification as a Full Professor of electrotechnics. In 2015, he was a Member of the Board of Professor of the Ph.D. course in metrology with Politecnico di Torino. Since 2018, he has been in the role of Deputy Coordinator. He is the author of more than 250 journal articles, with around 2700 citations (H-index 27). His research interests include computational electromagnetism for biomedical applications, with a main emphasis on MRI safety and medical devices. He is the INRiM contact person in the EURAMET Technical Committee of Interdisciplinary Metrology.